Electronic Supplementary Information

Sub-wavelength acoustic stencil for tailored micropatterning

Kirill Kolesnik,[a] Philipp Segeritz,[ab] Daniel J. Scott,[bc] Vijay Rajagopal,[a] David J Collins *[ad]

[a.] *Department of Biomedical Engineering, The University of Melbourne, Parkville, VIC 3010, Victoria, Australia.*
[b.] *The Florey Institute of Neuroscience and Mental Health, The University of Melbourne, 30 Royal Parade, Parkville, VIC 3052, Australia.*
[c.] *Department of Biochemistry and Pharmacology, The University of Melbourne, Parkville, VIC 3010, Australia.*
[d.] *The Graeme Clark Institute, The University of Melbourne, Parkville, VIC, 3010, Australia.*

**Corresponding author:* David J Collins
E-mail: david.collins@unimelb.edu.au

Supplementary Materials

The PDF file includes:

Other Supplementary Materials for this manuscript include the following:

Movies S1 to S5

Supplementary Figures

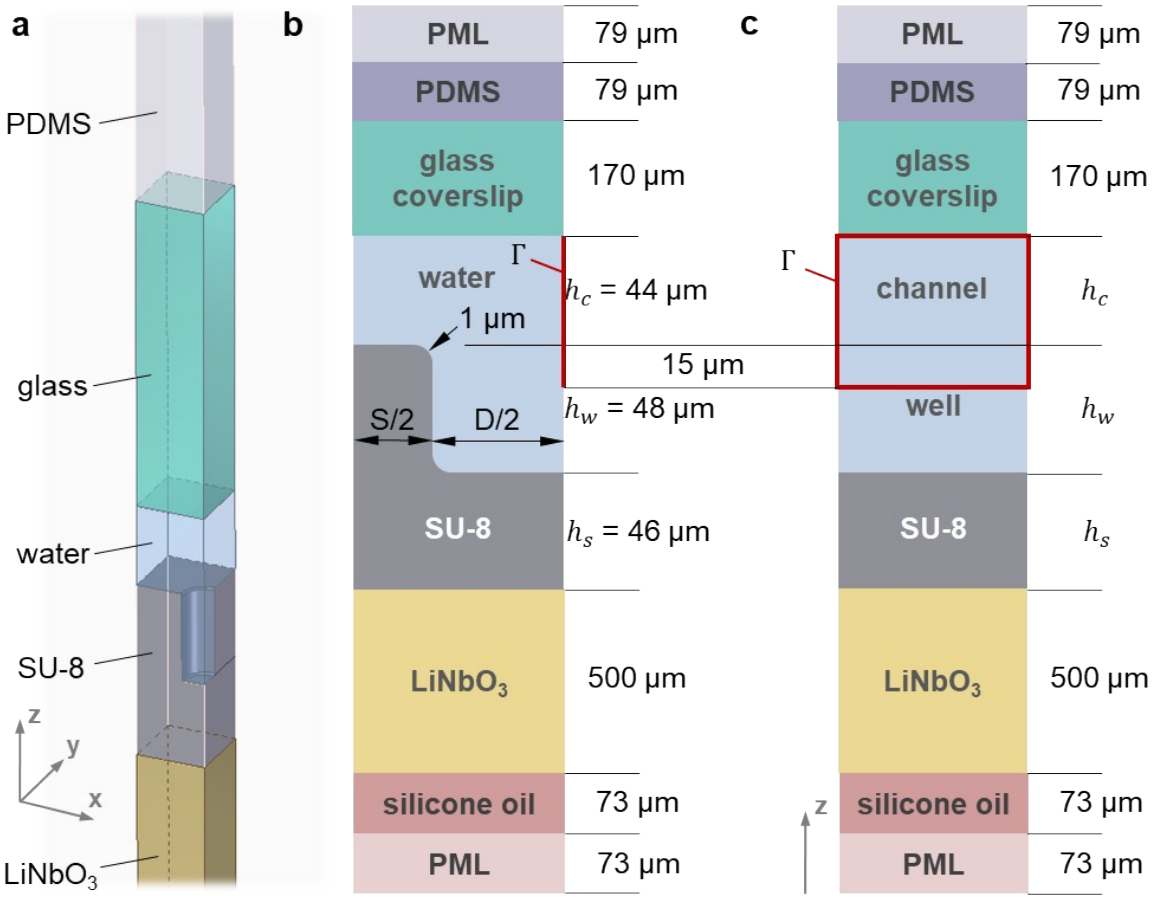

Fig. S1 Numerical simulation domains (a) The periodic structure with a quarter-microwell for the 3D study. (b) 3D computational domain cross-section (x-z view). (c) 1D simulation domain

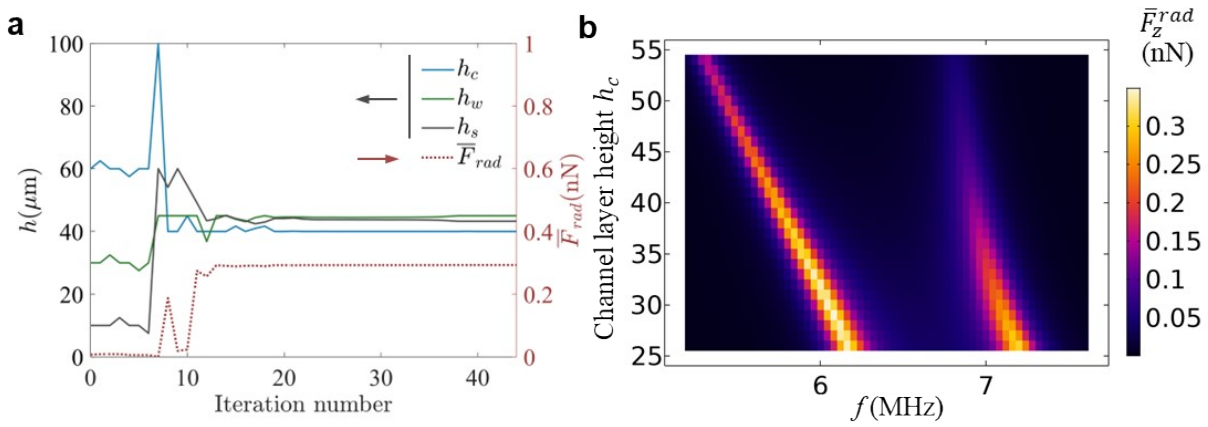

Fig. S2 Numerical analysis results. (a) Iterative numerical optimization using 1D model. (b) Averaged radiation force for domains of variable water layer height above the microwells and applied frequency f, showing both channel (left) and transducer (right) resonance peaks. Microwells in the parametric study have diameter D = 35 μm and spacing S = 15 μm.

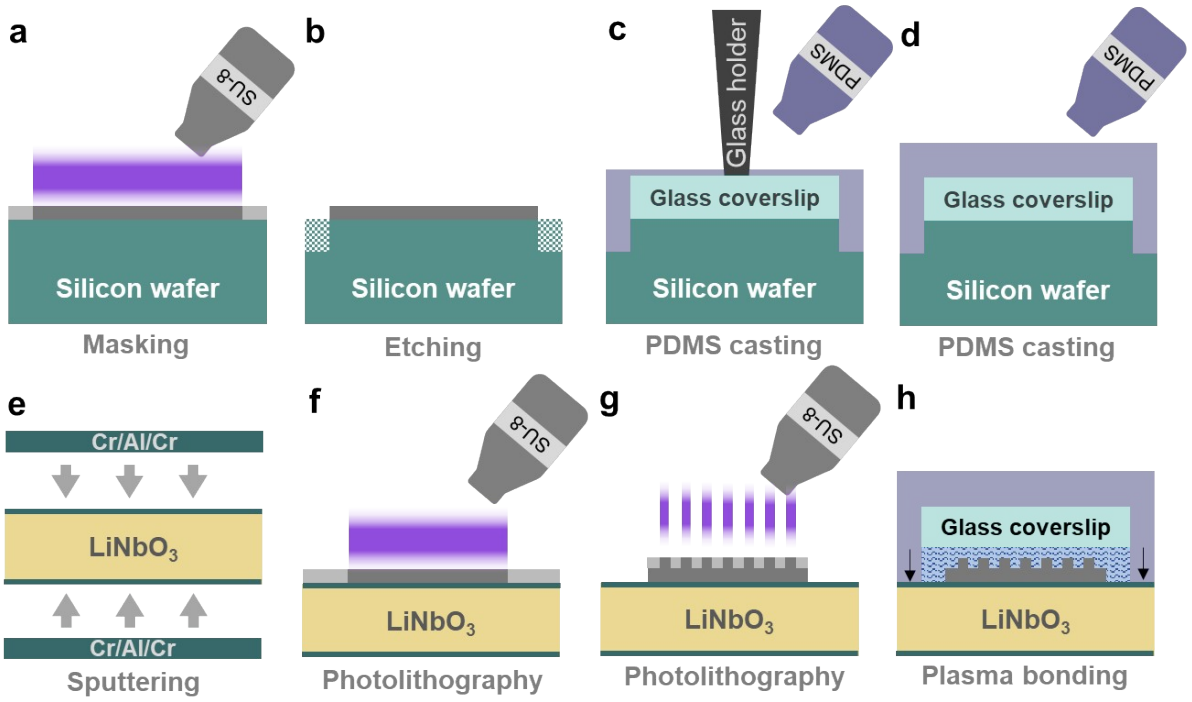

Fig. S3 Schematic depiction of microfluidic device fabrication steps, performed sequentially from a to h.

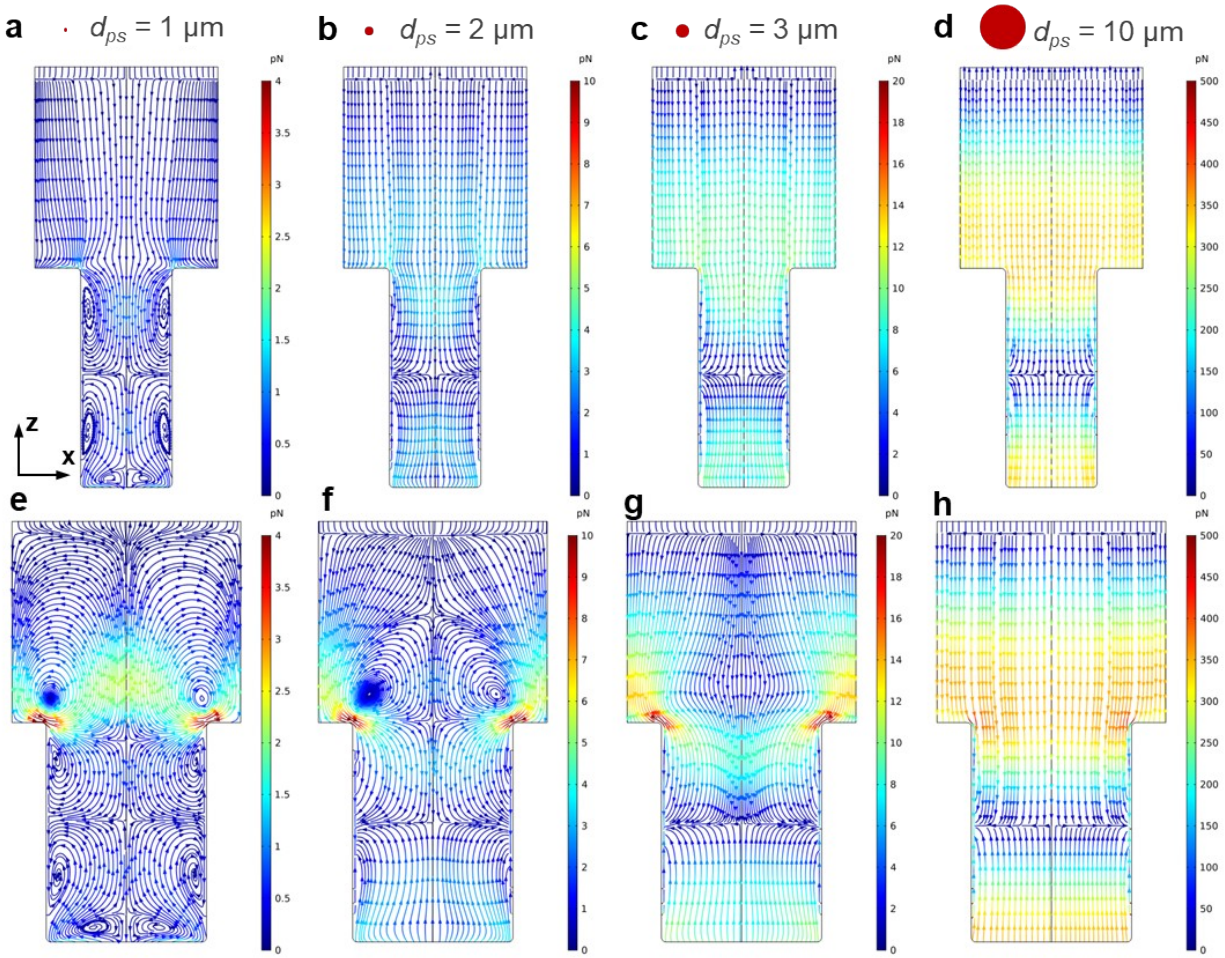

Fig. S4 Combined acoustic radiation and acoustic streaming-induced force and particle trajectories calculated for different particle sizes $d_{ps} = 1\ \mu m$ (a, e), $d_{ps} = 2\ \mu m$ (b, f), $d_{ps} = 3\ \mu m$ (c, g), $d_{ps} = 10\ \mu m$ (d, h) with D = 20 µm S = 20 µm (top row) and D = 35 µm, S = 15 µm (bottom row).

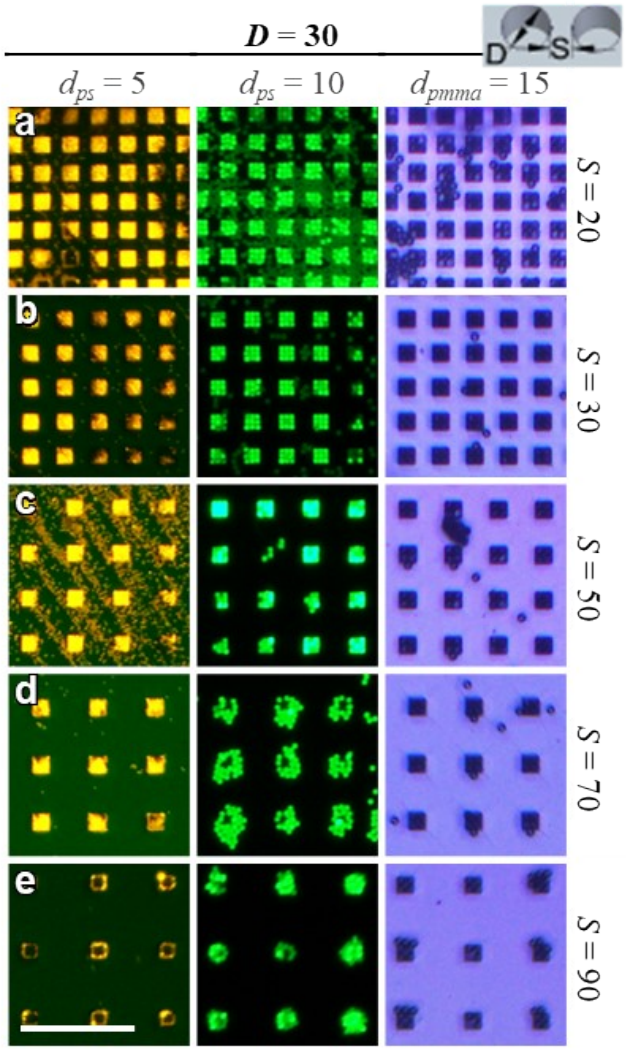

Fig. S5 Experimental particle trapping in square periodic cavities with width D = 30 μm and different spacing S. Rows (a-e) denote increasing S, with S = 20, 30, 50, 70 and 90 μm, respectively, in which 5 μm (yellow polystyrene), 10 μm (green polystyrene) and 15 μm non-fluorescent PMMA) particles are patterned. The actuation frequency is 5.8 MHz and driving voltage is $V_1 = 20\,V$. Sizes are in μm. Scale bar is 200 μm.

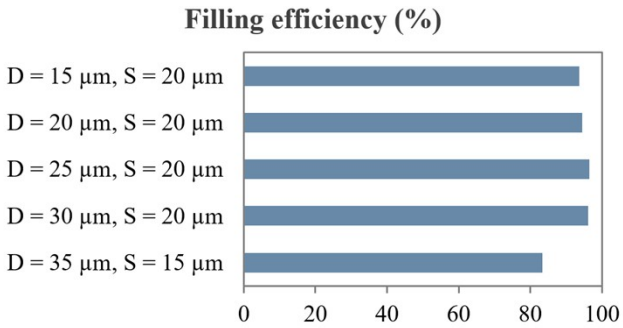

Fig. S6 The filling efficiency of circular microwells seeded with 15 µm PMMA microparticles.

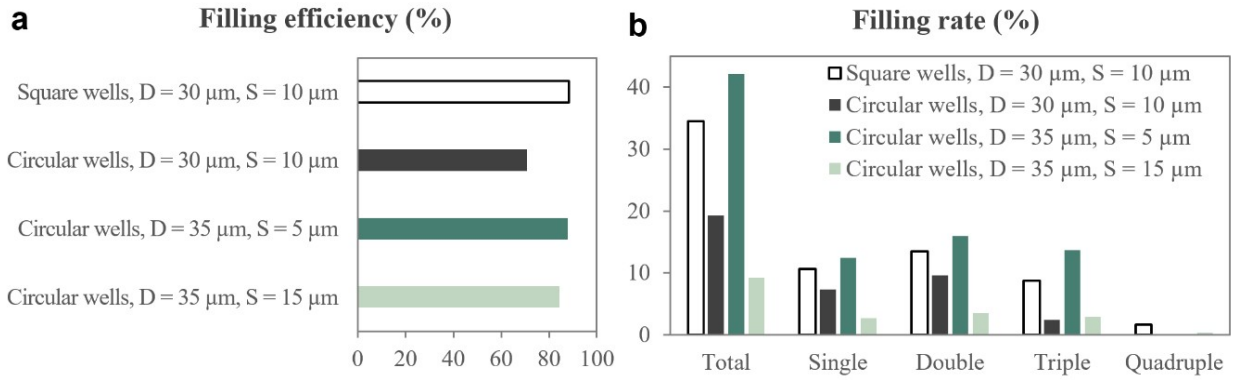

Fig. S7 293F cells capture in microwell arrays. (a) The filling efficiency of various well configurations. (b) Total-, single-, double-, triple- and quadruple-cell-per-well filling rates.

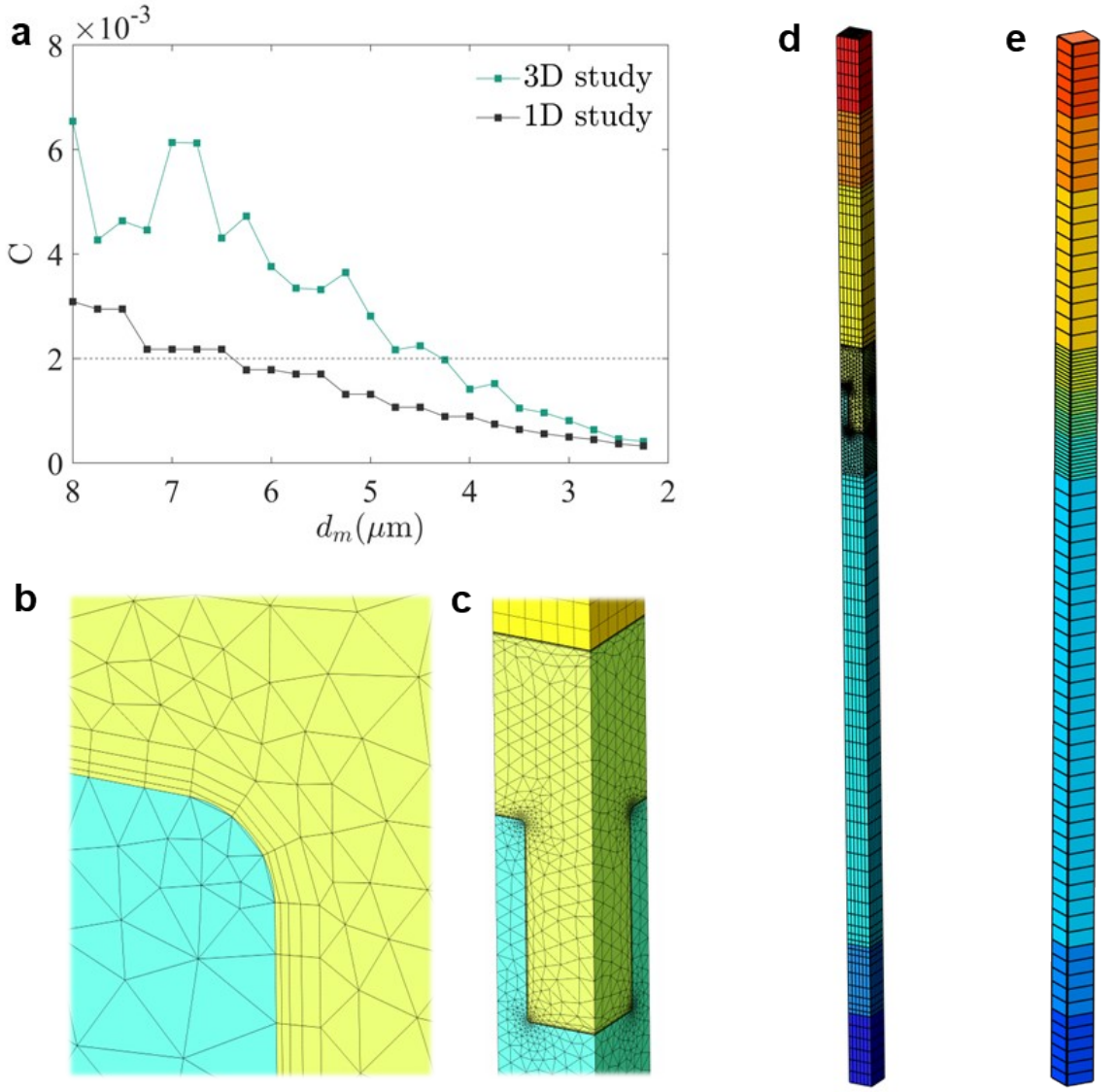

Fig. S8 Computational grid for the simulation domains (a) Mesh convergence study for the Gor'kov potential U_{rad} field in 3D and 1D studies. Dashed line indicates C = 0.002 threshold. (b-d) Computational mesh for the 3D study. (d) Close-up of the computational mesh for the fluid domain, with (c) showing the mesh elements at the fluid/solid boundary. (e) Computational grid for the 1D study.

Supplementary Movies

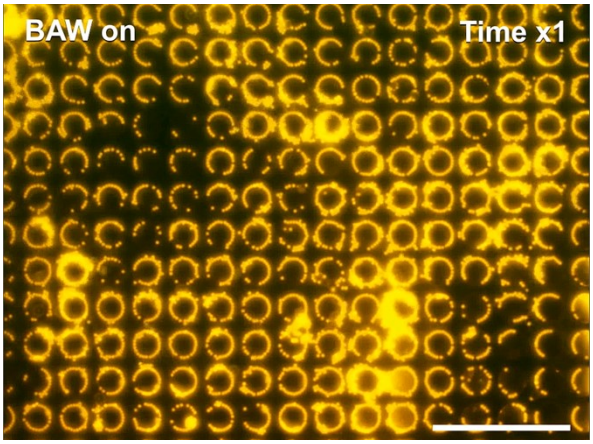

Movie S1 5 µm florescent particles focusing in welled array with diameter D = 35 and spacing S = 15 µm. Scale bar is 200 µm.

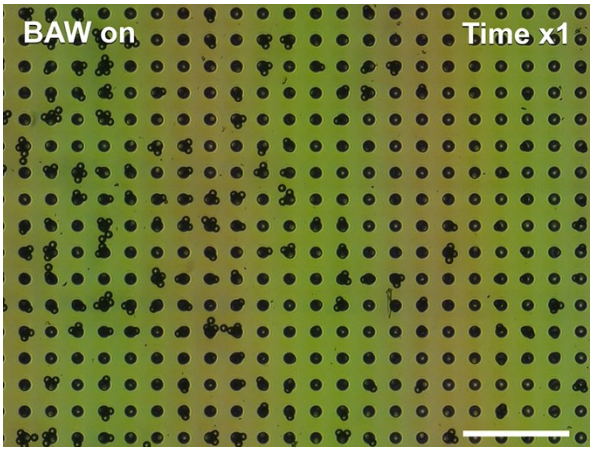

Movie S2 15 µm PMMA particles isolation with one particle per well in welled array with diameter D = 20 and spacing S = 30 µm. Scale bar is 200 µm.

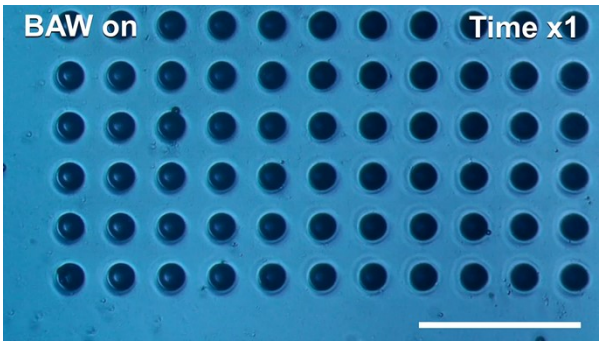

Movie S3 15 µm PMMA particles focusing in welled array with diameter D = 30 and spacing S = 30 µm. Scale bar is 200 µm.

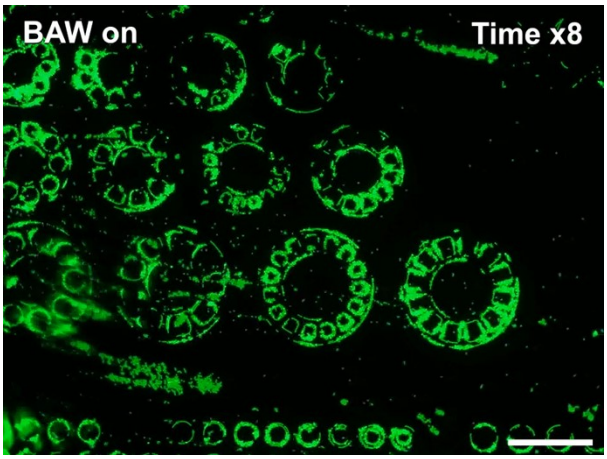

Movie S4 10 µm green fluorescent PS particles arrangement in bio-mimicking shapes. Scale bar is 500 µm.

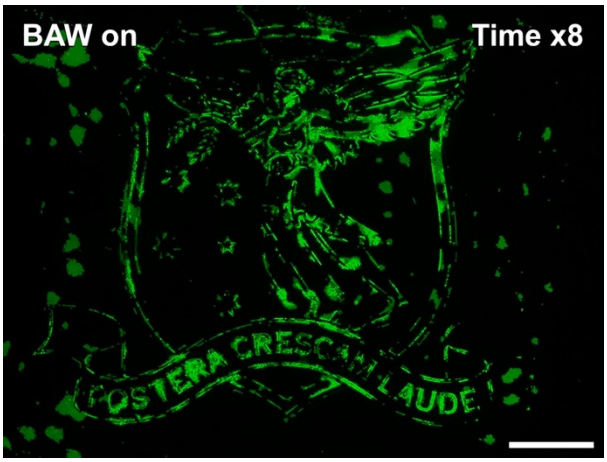

Movie S5 10 µm green fluorescent PS particles subsequent release and capture in shape of the University of Melbourne logo. Scale bar is 500 µm.

Supplementary Notes

Note S1.

Governing equations

The piezoelectric actuator is driven by a time-harmonic ac-voltage $V = V_1 e^{i\omega t}$ of amplitude V_1 and angular frequency $\omega = 2\pi f$, where f is the oscillation frequency. According to perturbation theory, physical fields can be decomposed to initial, first and second-order terms $g = g_0 + g_1 + g_2$, where 0-order term is the initial (background) condition. The first-order fields are time-dependent harmonic oscillations $g_1(r,t) = \bar{g}_1(r)e^{i\omega t}$ where $\bar{g}(r)$ is the complex valued amplitude. In the first step we solve the first order (linear) equations to generate maps of the acoustic potential fields. By utilizing the phase-dependent factor $e^{i\omega t}$, the time dependent solution can be produced.

The $LiNbO_3$ piezoelectric substrate was modelled with solid mechanics and electromechanical coupling. We introduce a Cartesian material coordinate system (X, Y, Z) to define constitutive equations and material properties for 128° rotated Y-cut $LiNbO_3$. Constitutive equations to describe the substrate relate the mechanical stress tensor σ_1 and the electric displacement field D_1 with the elastic displacement field u_1 and the electric potential φ_1. In the Voigt representation they are given by

$$\begin{pmatrix} \sigma_X \\ \sigma_Y \\ \sigma_Z \\ \sigma_{YZ} \\ \sigma_{XZ} \\ \sigma_{XY} \\ D_X \\ D_Y \\ D_Z \end{pmatrix} = \begin{pmatrix} C_{11} & C_{12} & C_{13} & C_{14} & 0 & 0 & 0 & -e_{21} & -e_{31} \\ C_{12} & C_{22} & C_{23} & C_{24} & 0 & 0 & 0 & -e_{22} & -e_{32} \\ C_{13} & C_{23} & C_{33} & C_{34} & 0 & 0 & 0 & -e_{23} & -e_{33} \\ C_{14} & C_{24} & C_{34} & C_{44} & 0 & 0 & 0 & -e_{24} & -e_{34} \\ 0 & 0 & 0 & 0 & C_{55} & C_{56} & -e_{15} & 0 & 0 \\ 0 & 0 & 0 & 0 & C_{56} & C_{66} & -e_{16} & 0 & 0 \\ 0 & 0 & 0 & 0 & e_{15} & e_{16} & \varepsilon_{11} & 0 & 0 \\ e_{21} & e_{22} & e_{23} & e_{24} & 0 & 0 & 0 & \varepsilon_{22} & \varepsilon_{23} \\ e_{31} & e_{32} & e_{33} & e_{34} & 0 & 0 & 0 & \varepsilon_{23} & \varepsilon_{33} \end{pmatrix} \begin{pmatrix} \partial_X u_X \\ \partial_Y u_Y \\ \partial_Z u_Z \\ \partial_Z u_Y + \partial_Y u_Z \\ \partial_Z u_X + \partial_X u_Z \\ \partial_Y u_X + \partial_X u_Y \\ -\partial_X \varphi \\ -\partial_Y \varphi \\ -\partial_Z \varphi \end{pmatrix}, \quad (2)$$

where C_{ij} are the elastic constants, ε_{ij} are the electric permittivities, and e_{ij} are the piezoelectric coupling constants. We introduce damping in the system through complex-valued elastic coefficients[1]

$$C_{ij} = C_{ij}^{'} + iC_{ij}^{''} = C_{ij}^{'}(1 + i\eta),\ \eta = \frac{1}{Q_m}, \quad (3)$$

where η is isotropic loss factor, Q_m is mechanical quality factor. Cauchy equation and Gauss's law for the piezoelectric substrate (without free charges) take form

$$\nabla \cdot \sigma_1 = -\rho_0 \omega^2 u_1, \quad (4)$$

$$\nabla \cdot D_1 = 0, \quad (5)$$

where ρ_0 is the mass density. The actuation of the piezoelectric electrodes is simulated using a terminal boundary condition with zero voltage on the bottom electrode and harmonic voltage with amplitude $V_1 = 20$ V on the top one.

We model the remaining non-piezoelectric solid domains (PDMS, glass, SU-8) as isotropic elastic materials. Constitutive equations for these domains include the Cauchy equation (4) and Hooke's Law, with

$$\begin{pmatrix}\sigma_x\\ \sigma_y\\ \sigma_z\\ \sigma_{yz}\\ \sigma_{xz}\\ \sigma_{xy}\end{pmatrix}=\begin{pmatrix}C_{11} & C_{12} & C_{12} & 0 & 0 & 0\\ C_{12} & C_{11} & C_{12} & 0 & 0 & 0\\ C_{12} & C_{12} & C_{11} & 0 & 0 & 0\\ 0 & 0 & 0 & C_{44} & 0 & 0\\ 0 & 0 & 0 & 0 & C_{44} & 0\\ 0 & 0 & 0 & 0 & 0 & C_{44}\end{pmatrix}\begin{pmatrix}\partial_x u_x\\ \partial_y u_y\\ \partial_z u_z\\ \partial_z u_z+\partial_y u_y\\ \partial_z u_z+\partial_x u_x\\ \partial_y u_y+\partial_x u_x\end{pmatrix}. \tag{6}$$

Considering mechanical damping through equation (3), storage modulus $C_{ij}^{'}$ in turn can be characterized by the longitudinal c_L and transverse c_T sound speeds, or Young's modulus E and the Poisson's ratio ν, with

$$C_{11}^{'}=c_L^2\rho_0=\frac{E(1-\nu)}{(1+\nu)(1-2\nu)}, \tag{7}$$

$$C_{44}^{'}=c_T^2\rho_0=\frac{E}{(1+\nu)}, \tag{8}$$

$$C_{12}^{'}=C_{11}^{'}-C_{44}^{'}. \tag{9}$$

A symmetry boundary condition was further applied on all side walls using

$$u_1\cdot n=0. \tag{10}$$

where n is the unit normal with respect to the boundary.

In the fluid domains (water, silicone oil), a set of linearized governing equations of continuity, energy, and momentum conservation is considered, with

$$\frac{\partial\rho_1}{\partial t}=-\rho_0\nabla\cdot v_1, \tag{11}$$

$$\frac{\partial T_1}{\partial t}=\nabla\left(D_T\nabla T_1\right)+\frac{\alpha T_0\,\partial\rho_1}{\rho_0 C_p\,\partial t}, \tag{12}$$

$$\rho_0\frac{\partial v_1}{\partial t}=-\nabla p_1+\beta\mu\nabla\left(\nabla\cdot v_1\right)+\mu\nabla^2 v_1, \tag{13}$$

where ρ_0 is the mass density, ρ_1 v_1, T_1, p_1 are 1st-order harmonic perturbation of density, velocity, temperature and pressure respectively, D_T is the thermal diffusivity of the liquid, α is the isobaric thermal expansion coefficient relating density change with temperature, $T_0=293.15\,K$ is the ambient temperature, C_p is the specific heat capacity at constant pressure, β is the viscosity ratio, relating the bulk (μ') and dynamic (μ) viscosities,[2] with $\beta=\frac{\mu'}{\mu}+\frac{1}{3}$. The equation of states formulates the constitutive relation between density, pressure and temperature:

$$\rho_1=\frac{p_1}{c^2}-\rho_0\alpha T_1, \tag{14}$$

where c is the sound speed. Since the silicone oil domain is facing a PML, we neglect heat transfer and viscous dissipation for this medium.

At the solid-fluid boundary the velocity was set to be continuous, with

$$v_1=-i\omega u_1. \tag{15}$$

A slip boundary condition was also applied on the outer side walls of the fluid domains to simulate a periodic array (symmetry condition), where

$$v_1\cdot n=0. \tag{16}$$

Finally, adiabatic boundary conditions on the fluid domain boundaries completes the numerical model, with

$$n\cdot\left(D_T\nabla T_1\right)=0. \tag{17}$$

We use a PML on the top and the bottom walls to mimic non-reflecting boundaries as shown in Fig. S1b,c. The PML acts as an artificial absorbing domain by imposing a complex-valued coordinate displacement in the z direction (polynomial stretching), with

$$\Delta z = \lambda\hat{z}(1-i) - h_{PML}\hat{z}, \tag{18}$$

where λ is acoustic wavelength, $\hat{z}$ is a local dimensionless coordinate, which varies from 0 to 1 over the PML height, where we set $h_{PML} = \lambda/2$ as the PML height.

Particles suspended in the fluidic channel are subject to a time-averaged acoustophoretic radiation force F^{rad}. For a spherical particle with diameter d_b, this is given by Gor'kov,[3] with

$$\begin{gathered} F^{rad} = -\nabla U^{rad},\ U^{rad} = V_{ps}\left(\frac{1}{2}f_1 k_w\langle p^2\rangle - \frac{3}{4}f_2\rho_{w,0}\langle v^2\rangle\right) \\ V_{ps} = \frac{\pi}{6}d_{ps}^3,\ f_1 = 1 - \frac{k_{ps}}{k_w},\ f_2 = \frac{2(\rho_{ps}-\rho_{0,w})}{2\rho_{ps}+\rho_{0,w}},\ k_w = \frac{1}{\rho_{w,0}c_w^2}, \end{gathered} \tag{19}$$

where U_{rad} is the Gor'kov potential, V_{ps} is a bead volume, f_1 and f_2 are monopole and dipole coefficients, k is compressibility, ρ is density, and the superscripts w and ps denotes water and polystyrene beads respectively. The bracketed quantities denote the time average over one oscillation period of the complex time-harmonic, where for fields A and B, $\langle AB\rangle = 0.5Re(A^*B)$, where the asterisk denotes complex conjugation. The expression (19) is valid for small particles compared to the fluidic wavelength, with $d_{ps} \ll \lambda_f$. At $7\ MHz$ the fluidic wavelength is $\lambda_f \sim 200$ um, where this expression is appropriate for the 5-15 μm diameter beads used in this study.

Since the Navier–Stokes governing equation are non-linear, harmonic actuation generates higher order responses. Following the perturbation theory, the second order time-averaged fields in the fluid domain $\langle g_2(r,t)\rangle$ can be calculated:

$$-\nabla\cdot\langle\rho_1 v_1\rangle = \rho_0\nabla\cdot v_2, \tag{20}$$

$$\rho_0\langle(v_1\cdot\nabla)v_1\rangle + \left\langle\rho_1\frac{\partial v_1}{\partial t}\right\rangle = -\nabla\langle p_2\rangle + \beta\mu\nabla(\nabla\cdot v_2) + \mu\nabla^2 v_2. \tag{21}$$

Hence the first-order fields drive the second-order time-averaged fields, termed acoustic streaming. To appropriately model the interaction of flowing fluid with structures, non-slip boundary conditions are applied at fluid-solid interfaces:

$$v_2 = 0, \tag{22}$$

and a slip boundary condition (symmetry condition) on the outer side walls (in the fluid domain):

$$v_2\cdot n = 0. \tag{23}$$

Note S2.

Mesh study

A hybrid computational mesh was used in the study, where fluid and SU-8 domains have a tetrahedral mesh and other domains have swept triangular prism mesh. A mesh convergence study was conducted using the approach from Devendran et al.[4] and Muller et al..[5] A convergence function $C(g)$ can be written as follows:

$$C(g) = \sqrt{\frac{\int \left(U_g^{rad} - U_{ref}^{rad}\right)^2 dx\, dy\, dz}{\int \left(U_{ref}^{rad}\right)^2 dx\, dydz}}, \tag{24}$$

where g is the current solution, U_{ref}^{rad} is a reference solution. Current and reference solutions have mesh element size of d_m and $d_{m,ref}$ respectively in the fluid and SU-8 domains with additional mesh refinement in the fluid boundary layer. Other domains have mesh elements not exceeding $4d_m$. The mesh study was performed for wells with diameter D = 20 μm and spacing of S = 20 μm at 5.56 MHz excitation. Fig. S8a. shows Gor'kov potential convergence in the fluid domain. Convergence threshold of $C < 0.002$ realized in a computational meshes with $d_m = 4.25$ μm used in this study (Fig. S8b-d and Fig. S8e.).

Note S3.

Half-wave resonance condition

The space between the piezoelectric substrate and glass coverslip can be treated as a half-wavelength resonator bounded by these two high acoustic impedance materials. This resonator comprises three layers and two materials, namely a uniform SU-8 photoresist layer, hybrid (cavity) layer and a water channel domain. The $LiNbO_3$/SU-8 and water/glass boundaries have high acoustic reflection due to strong acoustic impedance mismatch between the adjacent media. The half-wave resonance condition for such a multi-layered resonator can be derived using

$$f_{0.5} = \frac{0.5}{\sum_i \frac{h_i}{c_i}}, \tag{25}$$

where h and c are the height and speed of sound of the resonator components and $f_{0.5}$ is the half-wave resonance frequency. We define the effective speed of sound in the welled hybrid layer as an average of SU-8 and water properties considering their relative volume fraction

$$c_{hyb} = (c_{0,w} - c_{L,s})\frac{\pi}{4}\left(\frac{D}{S+D}\right)^2 + c_{L,s}, \tag{26}$$

where $c_{L,s}$ is longitudinal sound speed of SU-8 defined by (7).

Supplementary Tables

Table S1. Material properties used in the computational study

Material / Property	Notation	Value
Polydimethylsiloxane (PDMS) [6] [7]		
Density	$\rho_{0,p}$	1070 kg m^{-3}
Longitudinal wave speed	$c_{L,p}$	1030 m s^{-1}
Transverse (shear) wave speed	$c_{T,p}$	100 m s^{-1}
Loss factor	η_p	0.001
Pyrex (borosilicate) glass [7]		
Density	$\rho_{0,g}$	2230 kg m^{-3}
Longitudinal speed of sound	$c_{L,g}$	5591 m s^{-1}
Transverse speed of sound	$c_{T,g}$	3424m s^{-1}
Loss factor	η_g	0.001
Water [4]		
Density	$\rho_{0,w}$	997 kg m^{-3}
Sound speed	c_w	1497 m s^{-1}
Dynamic viscosity	μ	0.00089 Pa s
Bulk viscosity	μ'	0.00247 Pa s
Viscous boundary layer	$\delta_v = \sqrt{2\mu/\rho\omega}$	0.2 µm
Thermal conductivity	D_T	0.603 W m^{-1} K^{-1}
Specific heat capacity	C_p	4183 J kg^{-1} K^{-1}
Thermal expansion coefficient	α	0.000297 K^{-1}
SU-8 (3050)		
Density [8]	$\rho_{0,s}$	1153 kg m^{-3}
Young's Modulus [8]	E_s	2 Gpa
Poisson ratio [9]	ν_s	0.35
Loss factor [9]	η_s	0.023
$LiNbO_3$ (COMSOL Material library)		
Density	$\rho_{0,l}$	4700 kg m^{-3}
Elastic constants	C_{ij}	See Table S2.
Piezoelectric coupling constants	ε_{ij}	See Table S2.
Permittivity constants	e_{ij}	See Table S2.
Quality factor (experimentally acquired)	Q_l	59
Loss factor (experimentally acquired)	η_l	0.017
Silicone oil [10]		
Density	$\rho_{0,o}$	947 kg m^{-3}
Sound speed	c_o	1004 m s^{-1}
Polystyrene beads [11]		
Density	ρ_{ps}	1050 kg m^{-3}
Compressibility	k_{ps}	249 Tpa^{-1}
Diameter	d_{ps}	10 µm

Table S2. Lithium Niobate $LiNbO_3$ constants

Property	Notation	Value
Elastic constants	C_{11}, C_{22}	202.90 GPa
	C_{12}	52.92 GPa
	C_{13}, C_{23}	74.91 GPa
	C_{14}	9.00 GPa
	C_{24}	-9.00 GPa
	C_{33}	243.08 GPa
	C_{34}	0
	C_{44}, C_{55}	59.90 GPa
	C_{56}	8.99 GPa
	C_{66}	74.88 GPa
Piezoelectric coupling constants	e_{21}, e_{16}	-2.54 C m^{-2}
	e_{22}	2.54 C m^{-2}
	e_{23}, e_{34}	0
	e_{24}, e_{15}	3.70 C m^{-2}
	e_{31}, e_{32}	0.19 C m^{-2}
	e_{33}	1.31 C m^{-2}
Permittivity constants	ε_{11}, ε_{22}	43.6
	ε_{23}	0
	ε_{33}	29.16

References

1 P. Hahn, O. Schwab and J. Dual, *Lab Chip*, 2014, **14**, 3937–3948.
2 J. S. Bach and H. Bruus, *J Acoust Soc Am*, 2018, **144**, 766–784.
3 L. P. Gor'kov, in *Sov. Phys. Dokl.*, 1962, vol. 6, pp. 773–775.
4 C. Devendran, T. Albrecht, J. Brenker, T. Alan and A. Neild, *Lab Chip*, 2016, **16**, 3756–3766.
5 P. B. Muller, R. Barnkob, M. J. H. Jensen and H. Bruus, *Lab Chip*, 2012, **12**, 4617–4627.
6 Z. Ni, C. Yin, G. Xu, L. Xie, J. Huang, S. Liu, J. Tu, X. Guo and D. Zhang, *Lab Chip*, 2019, **19**, 2728–2740.
7 N. R. Skov and H. Bruus, *Micromachines (Basel)*, 2016, **7**, 1–14.
8 Microchem, *Product Datasheet*, , DOI:10.1146/annurev.matsci.28.1.153.
9 S. Chung and S. Park, *Journal of Mechanical Science and Technology*, 2013, **27**, 2701–2707.
10 I. Leibacher, P. Reichert and J. Dual, *Lab Chip*, 2015, **15**, 2896–2905.
11 M. Tayebi, R. O'Rorke, H. C. Wong, H. Y. Low, J. Han, D. J. Collins and Y. Ai, *Small*, 2020, **2000462**, 1–9.